

# Optical tomography of a realistic neonatal head phantom

Adam Gibson, Roza Md. Yusof, Hamid Dehghani, Jason Riley, Nick Everdell, Robin Richards, Jeremy C. Hebden, Martin Schweiger, Simon R. Arridge, and David T. Delpy

We have begun clinical trials of optical tomography of the neonatal brain. To validate this research, we have built and imaged an anatomically realistic, tissue-equivalent neonatal head phantom that is hollow, allowing contrasting objects to be placed inside it. Images were reconstructed by use of two finite-element meshes, one generated from a computed tomography image of the phantom and the other spherical. The phantom was filled with a liquid of the same optical properties as the outer region, and two perturbations were placed inside. These were successfully imaged with good separation between the absorption and scatter coefficients. The phantom was then refilled with a liquid of increased absorption compared with the background to simulate the brain, and the absolute properties of the two regions were found. These were used as *a priori* information for the complete reconstruction. Both perturbations were visible, superimposed on the increased absorption of the central region. The head-shaped mesh performed slightly better than the spherical mesh, particularly when the absorption of the central region of the phantom was increased. © 2003 Optical Society of America

OCIS codes: 170.3880, 170.6920.

## 1. Introduction

The great advances in medical imaging during the past 20 years have had only a limited effect on the routine clinical care of newborn babies because of the size and cost of magnetic resonance imaging (MRI) and computed tomography (CT) scanners and because of the difficulty of transporting severely ill infants to the scanner. There is a clinical need for a portable, bedside system that can produce three-dimensional (3D) images of the neonatal head to assist in the identification of hemorrhage and hypoxia-ischaemia and the monitoring of treatment. Optical tomography is sensitive to changes in blood oxygen saturation and blood volume and could, in principle, fill this niche. In addition, images obtained with optical tomography contain information

about the physiology of the tissue, as opposed to MRI, CT, and ultrasound, which generally provide anatomical information.

A number of workers have demonstrated brain imaging using optical topography, in which measurements are made from detectors close to the active source, allowing fast data acquisition. Optical tomography of the neonatal brain has been successfully performed by a number of groups.<sup>1-5</sup> Generally, these data are displayed as two-dimensional (2D) maps of cortical activation without depth discrimination, although Bluestone *et al.*<sup>6</sup> reconstructed 3D images of the frontal region of the adult brain by use of sources and detectors positioned on the forehead.

If the sources and detectors are spaced around the object of interest, the whole volume can be sampled and tomographic images showing the optical properties of the entire object can be reconstructed. 2D optical tomography of the neonatal head from a ring of sources and detectors was first demonstrated by Benaron *et al.*<sup>2</sup> At University College London, we have developed instrumentation<sup>7</sup> and reconstruction software<sup>8</sup> with the specific aim of generating images from the neonatal head and have recently recorded fully 3D data from a baby's head for the first time to our knowledge.<sup>9</sup>

Many groups have tested their optical tomography systems using tissue-equivalent phantoms.<sup>10-12</sup> Typically, phantoms are cylindrical so that the effect

---

A. Gibson (agibson@medphys.ucl.ac.uk), R. Md. Yusof, N. Everdell, R. Richards, J. C. Hebden, and D. T. Delpy are with the Department of Medical Physics and Bioengineering, and J. Riley, M. Schweiger, and S. R. Arridge are with the Department of Computer Science, University College London, 11-20 Capper Street, London WC1E 6JA. H. Dehghani is with Thayer School of Engineering, Dartmouth College, 8000 Cummings Hall, Hanover, New Hampshire 03755-8000.

Received 22 July 2002; revised manuscript received 24 October 2002.

0003-6935/03/163109-08\$15.00/0

© 2003 Optical Society of America

of instrumentation and reconstruction techniques can be examined independently of errors caused by difficulties in generating and solving finite-element meshes of complex structures. Recently, more anatomically realistic phantoms have been used, such as a conical phantom to represent the breast.<sup>13</sup>

To support the clinical research, we have made and imaged a tissue-equivalent optical phantom cast in the shape of the neonatal head. Two different finite-element meshes were used to reconstruct the data: a realistic head-shaped mesh, taken from a CT scan of the phantom, and a spherical mesh. The main reasons for performing these studies were to develop and validate a technique for imaging the neonatal head and to examine the effects of the complex geometry of the head on the quality of the image reconstruction. In clinical studies the surface geometry of the head and the positions of the optodes could be determined from a MR image of the baby, although for ill babies this may be clinically unacceptable.

## 2. Method

A tissue-equivalent optical phantom of the neonatal head was cast in epoxy resin<sup>14</sup> from a mold made from an anatomically realistic doll. The circumference was 24 cm, corresponding to a baby of ~26 weeks gestation. The optical properties were controlled by addition of titanium dioxide (which provides scatter) and a near-infrared absorbing dye. The properties of the head, especially the neonatal head, are not particularly well known. The absorption and transport scatter coefficients of the neonatal brain at 800 nm are approximately 0.02 and 0.7 mm<sup>-1</sup>, respectively.<sup>15</sup> The skin has lower absorption ( $\mu_a \approx 0.01$  mm<sup>-1</sup>) and higher scatter ( $\mu_s' \approx 1.5$  mm<sup>-1</sup>) than the brain,<sup>16</sup> whereas the properties of the neonatal skull are largely unknown. These values were all measured *ex vivo*, and it is expected that these values will be different *in vivo*, especially the absorption of the brain, which is expected to be higher because of the high vascularization. The phantom was hollow, with the outer shell corresponding to the scalp and skull, and the inner spherical hollow region, the brain. The outer shell was assigned optical properties of  $\mu_a = 0.01$  mm<sup>-1</sup> and  $\mu_s' = 1.0$  mm<sup>-1</sup> at 780 nm. During experiments, the hollow region was filled with epoxy resin without hardener, so it remained liquid. Measurement of the refractive index,  $n$ , of the solid and the liquid resin showed that they agree to within 1% ( $n = 1.56$  at 780 nm). Two different batches of liquid resin were used, one with properties equal to those of the outer region and the other with increased absorption to simulate the brain.

Our optical imaging system is known as MONSTIR (multichannel optoelectronic near-infrared system for time-resolved image reconstruction<sup>7</sup>). A portable fiber laser (IMRA Incorporated) produces pulses of ~2-ps duration at wavelengths of 780 and 815 nm, interlaced at 80 MHz. These pulses are coupled, by means of a 32-way optical switch that illuminates each source fiber in sequence, onto the surface of the object being studied. The laser power at the tip of a

source fiber is approximately 15 mW. Each source fiber is paired with a detector fiber bundle, and both are held 10 mm from the surface of the object by a connector.<sup>17</sup> Light that has diffused through the object is collected simultaneously by the remaining detector fiber bundles and coupled to four 8-anode microchannel-plate photomultiplier tubes (MCP-PMTs), which are protected from overexposure by a series of programmable variable optical attenuators. The MCP-PMTs produce an electronic pulse for each detected photon.

The arrival time of each photon is measured relative to a reference signal from the laser, allowing a histogram of flight times (called a temporal point-spread function or TPSF) to be built up for each source-detector pair.

A helmet was constructed to hold 29 connectors, each holding a source and a detector fiber, onto the phantom rigidly such that each optode was optically isolated from every other optode. The helmet was made from thermoplastic (WFR/Aquaplast Corporation) and black, near-infrared absorbing foam (RS Components Ltd.), with holes cut to insert the optodes. Nylon screws held the helmet onto the phantom so that it could be removed and replaced in exactly the same position. It is important for accurate image reconstruction that the optode positions are known and that they remain fixed throughout the experiment.

A helical CT scan was taken of the phantom and helmet with a spatial resolution of ~0.5 mm. A 3D CT image was generated [see Fig. 1(a)] with software written in-house ([www.medphys.ucl.ac.uk/research/mgi/manual/3dintro.htm](http://www.medphys.ucl.ac.uk/research/mgi/manual/3dintro.htm)). This software treats the CT data as an array of gray-scale voxels. The surface of the phantom was extracted by means of defining an interpolated iso-surface through the volume at a threshold that was set approximately halfway between the mean gray-scale value inside the phantom and that outside. This surface was saved as a triangular mesh. The optode positions were defined as landmarks on the surface of the phantom by extrapolation from the location of the optodes in the helmet. This gave an accurate surface outline and enabled the optode positions to be known to within ~0.5 mm.

The surface mesh was processed with the Visualization Toolkit (Kitware, Incorporated) and a volume finite-element mesh produced with Netgen,<sup>18</sup> which is based on an advancing front algorithm. The mesh had 12201 quadratic elements—the average element volume was 23 mm<sup>3</sup>, and the largest was 69 mm<sup>3</sup> [Fig. 1(b)]. The sphere that best fitted the measured optode positions was found by use of a Gauss-Newton fitting technique ([www.npl.co.uk/ssfm/metros/key\\_functions/](http://www.npl.co.uk/ssfm/metros/key_functions/)), and a finite-element mesh was generated from this spherical model. It had 12,743 quadratic elements, with an average volume of 17 mm<sup>3</sup> and a maximum of 129 mm<sup>3</sup>. Both meshes were tested by generation of simulated photon density maps. The mesh was deemed to be acceptable if

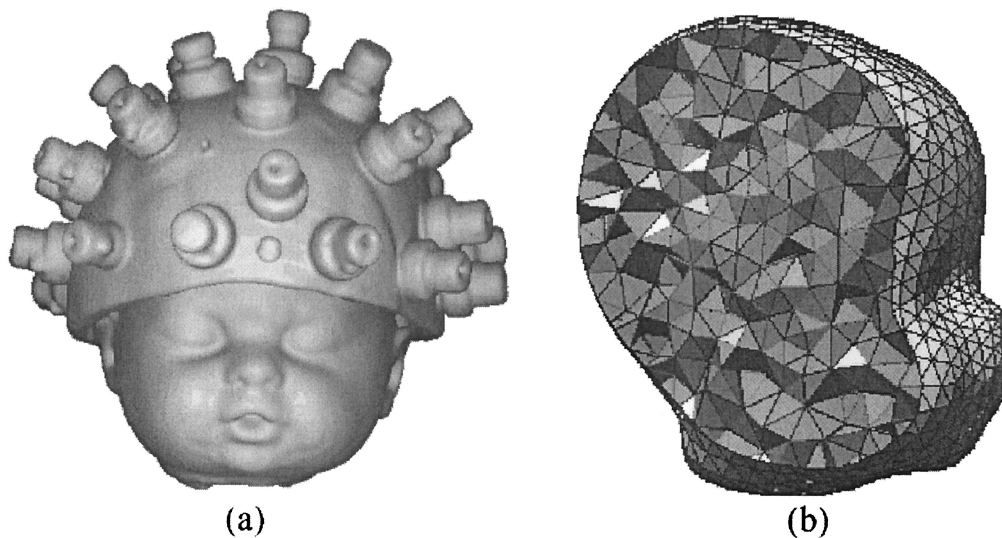


Fig. 1. (a) 3D CT image of the phantom and helmet; (b) head-shaped finite element mesh, with the surface cut away to show the internal structure.

the photon density was positive and smooth everywhere.

The phantom was first filled with liquid resin with the same properties as the solid outer shell ( $\mu_a = 0.01 \text{ mm}^{-1}$ ;  $\mu'_s = 1.0 \text{ mm}^{-1}$ ). Two epoxy resin cylinders, of height and diameter 7 mm, were suspended on thin wires within the upside-down phantom (see Fig. 2), one with  $\mu_a = 0.05 \text{ mm}^{-1}$  and  $\mu'_s = 1.0 \text{ mm}^{-1}$ , and the other with  $\mu_a = 0.01 \text{ mm}^{-1}$  and  $\mu'_s = 5.0 \text{ mm}^{-1}$ . An image data set and then a reference set without the two cylinders present were acquired with 29 sources illuminated sequentially for 10 s with between 20 and 26 detectors active for each source. This is referred to as the *homogeneous phantom*. The phantom was then refilled with liquid resin with increased absorption ( $\mu_a = 0.015 \text{ mm}^{-1}$ ;  $\mu'_s = 1.0 \text{ mm}^{-1}$ ) to simulate the higher absorption of the brain compared with the scalp and skull. Another pair of image data sets was

acquired from this *inhomogeneous phantom*, both with and without the two cylinders present. The properties of the phantoms were not dependent on wavelength, so only data collected at 780 nm were used for reconstructions.

Images were reconstructed with the TOAST (temporal optical absorption and scattering tomography<sup>8</sup>) image-reconstruction software, developed at University College London. TOAST solves the forward problem using the finite-element method to generate simulated measurements for a given distribution of internal scattering and absorption parameters. The inverse problem is then solved iteratively and non-linearly by adjustment of the internal parameters until the simulated measurements match the experimental data. To reduce the reconstruction time, TOAST does not calculate TPSFs; instead, datatypes such as log intensity and mean time are generated directly from the finite-element model and compared with the equivalent data types extracted from the measured TPSFs. In this study, images were reconstructed from the ratios of intensities and the differences in mean photon flight times between the data set with the two cylinders and the reference data set. The use of a reference image data set reduces the effect of uncertainties in the head shape or optode positions, as well as measurement errors. Clinically, such data could be acquired on a separate phantom, or by means of acquiring data before and after a physiological event such as an evoked response. Using both intensity ratio and mean-time difference as data types allows separate images to be reconstructed that distinguish between absorption and scatter coefficients. Images were generated for both the head-shaped and the spherical finite-element meshes. It took  $\sim 30$  min to reconstruct each iteration on a 1.4-GHz Athlon computer with 1-Gbyte of RAM. After 25 iterations, no further improvement

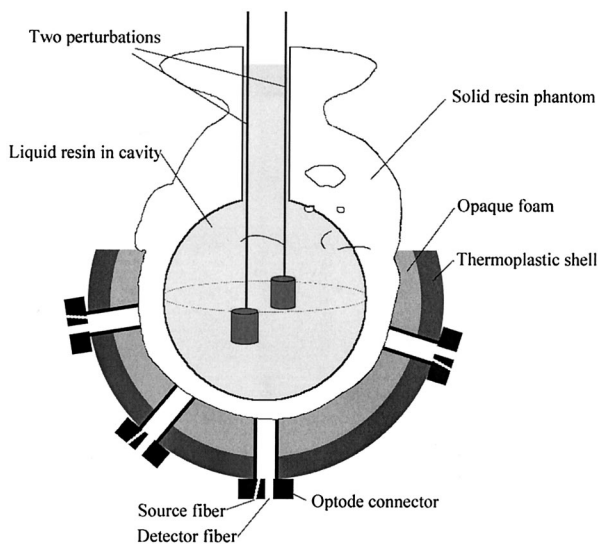


Fig. 2. Schematic diagram of the experimental method.

in image quality was seen, and the reconstructions were terminated.

The initial conditions for the reconstruction of images of the homogeneous phantom were taken from the best estimates of the phantom's background properties, which were  $\mu_a = 0.01 \text{ mm}^{-1}$  and  $\mu_s' = 1.0 \text{ mm}^{-1}$ . The inhomogeneous phantom was reconstructed with a two-step process. The phantom was assumed to consist of two piecewise constant regions with known boundaries but unknown optical properties, corresponding to the information that could be expected clinically from an anatomical MR image. In this study the boundary of the internal region was estimated from the known diameter of the hollow spherical region. The absolute properties of the piecewise constant regions can be reconstructed on the low-dimensional region basis, before these results are used as starting conditions for a second reconstruction to solve for the perturbations.<sup>19</sup> This technique was used to calculate the properties of the two regions, with absolute mean photon flight time and variance as datatypes. Absolute intensity cannot be used for reconstruction, since it is highly sensitive to the surface coupling between the optodes and the phantom. A similar approach was taken by Ntzichristos *et al.*,<sup>20</sup> who used *a priori* information taken from a MR image for image reconstruction during near-infrared spectroscopy.

### 3. Results

Figure 3 shows images of scatter and absorption reconstructed from data acquired from the homogeneous phantom with the two finite-element meshes. The two sets of images are similar, with the same features visible in each. For both meshes, the scattering and absorbing cylinders can each be seen in the appropriate image, together with some limited cross talk from the other perturbation. In this study the *absorption contrast* was defined as the ratio of the peak absorption to the background and the *scatter contrast* as the ratio of the peak scatter to the background. The absorption and scatter contrasts are both 1.2 for both the head-shaped and the spherical meshes, significantly underestimating the actual contrast in all four images.

Images of the inhomogeneous phantom, reconstructed with the same starting conditions as with the homogeneous phantom, are shown in Fig. 4. In this case, the head-shaped finite-element mesh performs qualitatively better than the spherical mesh. In Fig. 4(a), both features are visible, although both appear to be closer to the center of the phantom than their actual positions. However, Fig. 4(b) is dominated by an artifact that appears to originate from an optode. The absorption contrast is 1.2 for both sets of images, whereas the scatter contrast was reduced to 1.1.

The calculated properties for the two regions of the phantom are shown in Table 1. In general, the correct values have been recovered to an accuracy of better than 8%. However, reconstruction on the realistic mesh gave a substantially larger error (25%)

for the absorption in the skull and scalp region than the spherical mesh. Figure 5 shows images reconstructed starting from these calculated values. Both features can be clearly seen, with the absorption feature superimposed on a central region of increased absorption. The localization of the perturbations is significantly better for the head-shaped mesh than for the spherical, which appears to put the peak change close to the center of the mesh. The absorption contrasts relative to the central and outer regions are 1.1 and 1.6, respectively, for the head-shaped mesh, and 1.1 and 1.4 for the spherical mesh. The scatter contrast for both meshes is 1.1.

### 4. Discussion

This study has shown that images can be reconstructed from a realistic complex 3D geometry, such as the head. Features within these images can be accurately localized, and good separation between changes in absorption and scatter coefficients can be obtained if both intensity ratio and mean-time difference datatypes are used (Fig. 3). However, the contrast is severely underestimated. This is partly due to a partial volume effect caused by the limited resolution, but the contrast could be improved by appropriate regularization in the reconstruction process.

Furthermore, the results have shown that successful 3D reconstruction of features within a model containing regions of different optical parameters is possible. The perturbations can be clearly seen, even if no *a priori* information is used in the reconstruction algorithm (Fig. 4). In addition, information about the location of the regions can be used to calculate the absolute properties of the two regions (Table 1) that, when used as the initial values for the reconstruction, allows the perturbation to be reconstructed on top of the background properties of the two regions (Fig. 5). However, as the reconstruction tends to underestimate the amplitude of the perturbation change, when this reduced value is superimposed on the properties of the central region, its contrast compared with the increased background absorption is low.

Images were successfully reconstructed from the spherical mesh, particularly from the homogeneous phantom, where the spherical mesh performed as well as the head-shaped mesh. It appeared that as the phantom and reconstruction process became more complex, more benefit was seen from using the realistic mesh. However, in all cases, the advantage of using the realistic mesh was less than might be expected. One reason for this is that whereas the surface of the realistic mesh and the optode positions were obtained independently from the CT image, the spherical mesh was actually optimized so that it gave the best possible fit to the measured optode positions. TOAST models the light sources as points positioned one transport scattering length beneath the surface.<sup>21</sup> To do this, the sources are shifted from their original position. The average distance TOAST had to shift the sources so that they lay 1 mm beneath the surface of the head-shaped mesh was 1.6 mm (the maximum shift was 2.6

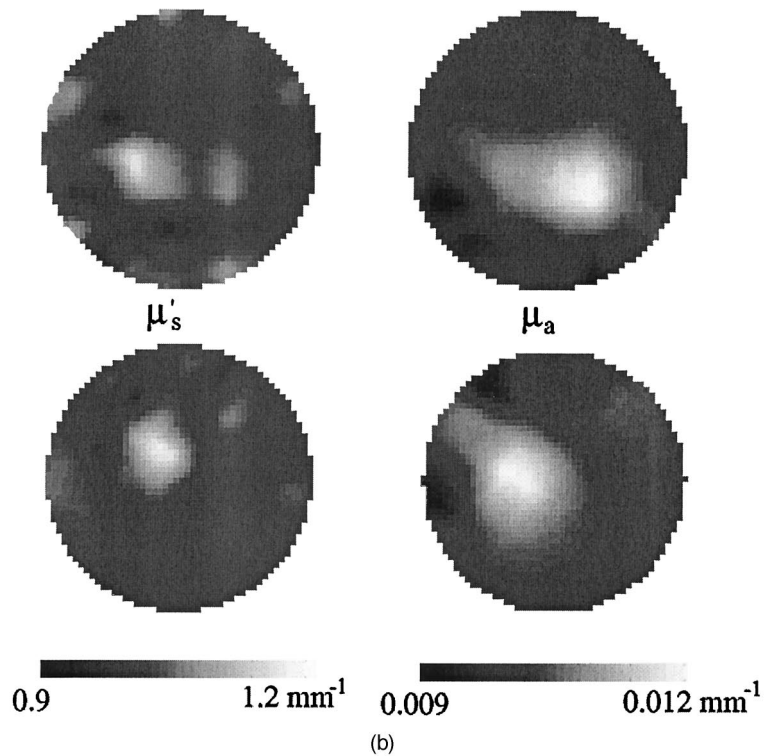
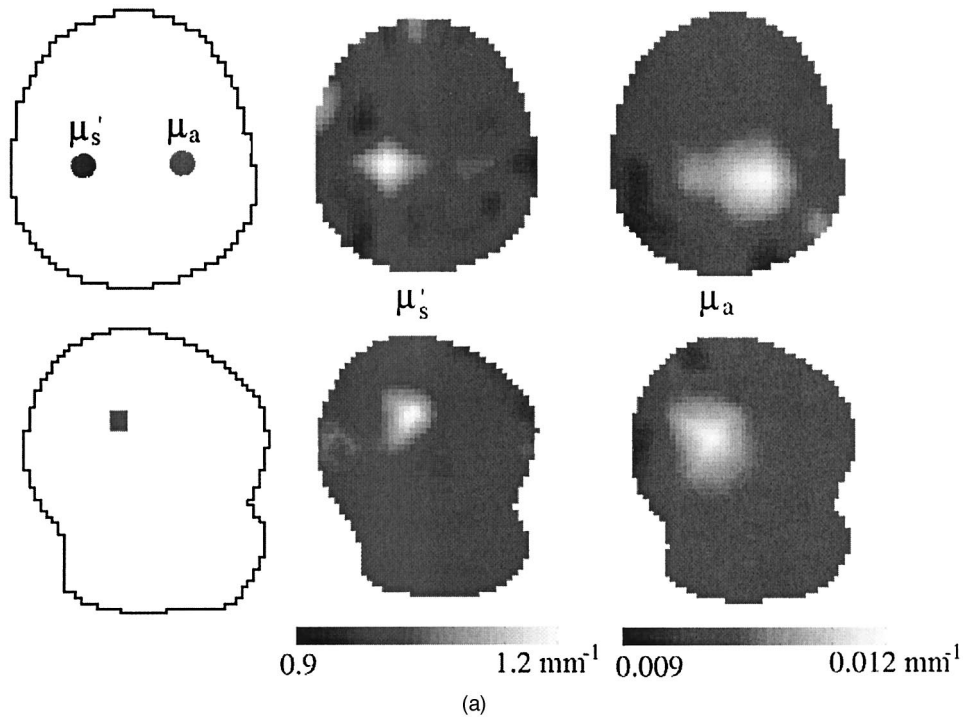


Fig. 3. (a) Reconstruction of homogeneous phantom onto the head-shaped finite-element mesh. The top row shows transverse slices and the bottom row sagittal slices through the 3D image. The left-hand column is a schematic representation of the phantom showing the approximate location of the perturbations. The middle and right-hand columns show the scatter and absorption images, respectively. (b) Reconstruction of homogeneous phantom onto the spherical finite-element mesh. The slices are the same as those in the head-shaped mesh.

mm), whereas for the spherical mesh, TOAST had to move the optodes by only 1.2 mm (maximum 2.4 mm), suggesting that in some respects, the spherical mesh gave a better fit to the measured optode positions than

the head-shaped mesh. We are currently developing methods to optimize the head-shaped mesh by fitting it to the measured optode positions. This should improve its performance compared with that of the spher-

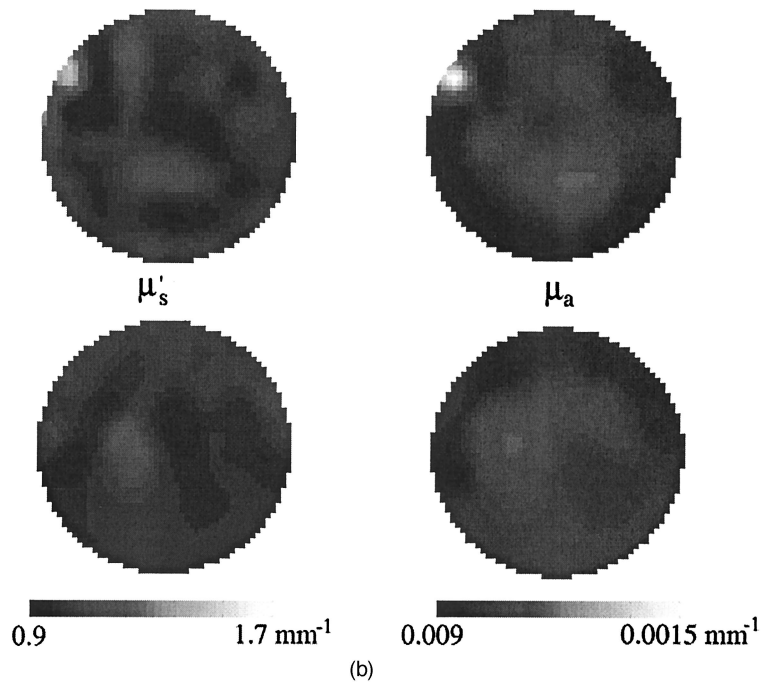
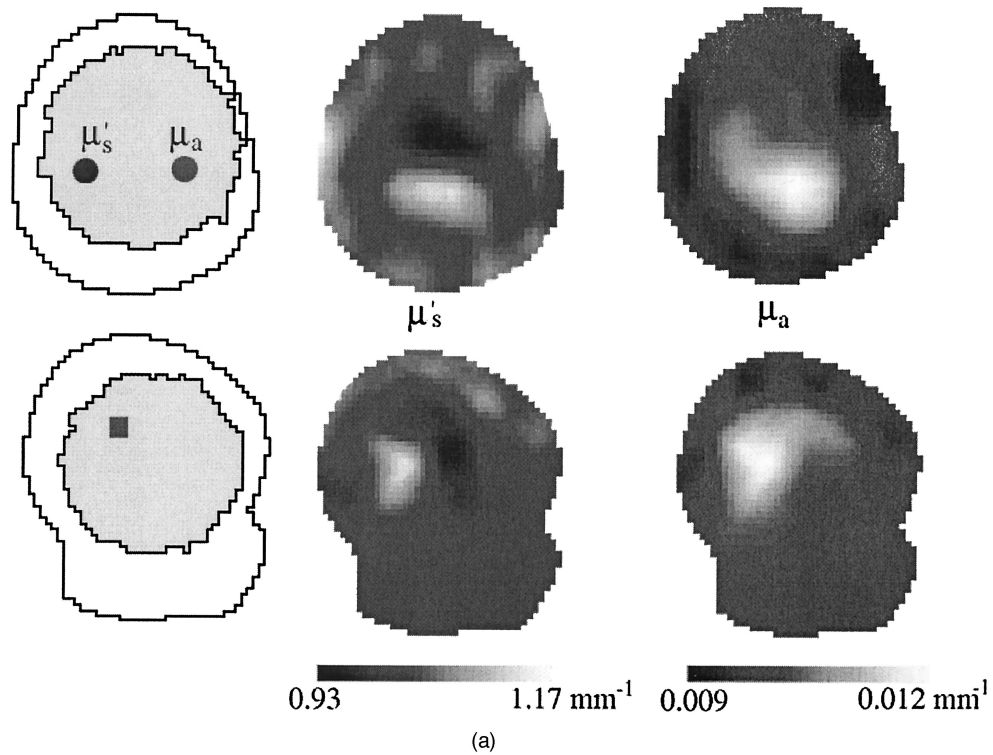


Fig. 4. (a) Reconstruction of the inhomogeneous phantom onto the head-shaped finite-element mesh, with homogeneous starting conditions. (b) Reconstruction of the inhomogeneous phantom onto the spherical finite element mesh, with homogeneous starting conditions.

Table 1. Expected and Calculated Properties of the Two Regions in the Inhomogeneous Phantom

		Expected/mm <sup>-1</sup>	Calculated for Head Model/mm <sup>-1</sup>	Calculated for Spherical Model/mm <sup>-1</sup>
Scalp and skull	$\mu_a$	0.01	0.012	0.01
	$\mu'_s$	1.0	1.08	1.05
Brain	$\mu_a$	0.015	0.016	0.016
	$\mu'_s$	1.0	0.99	0.93

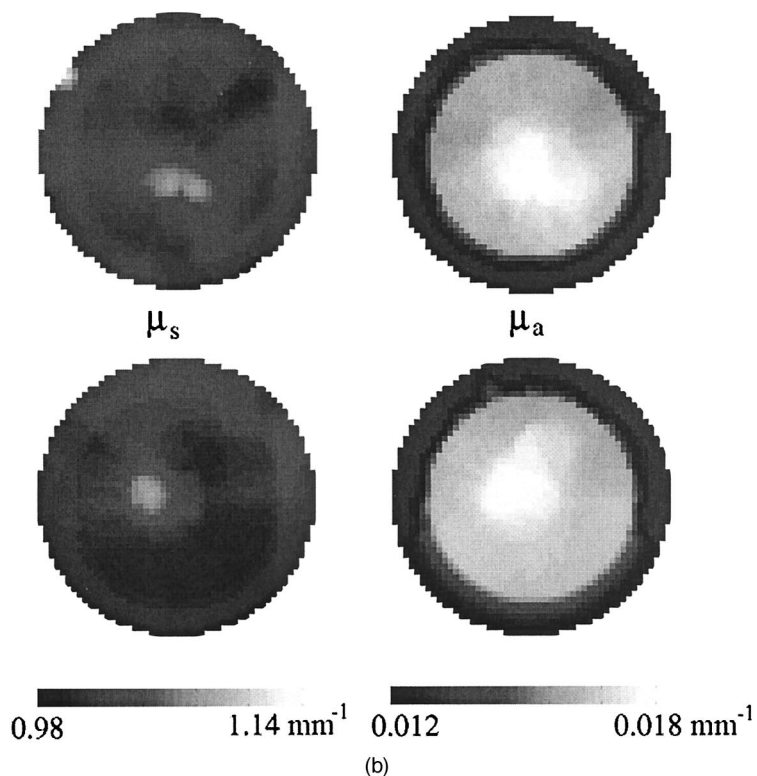
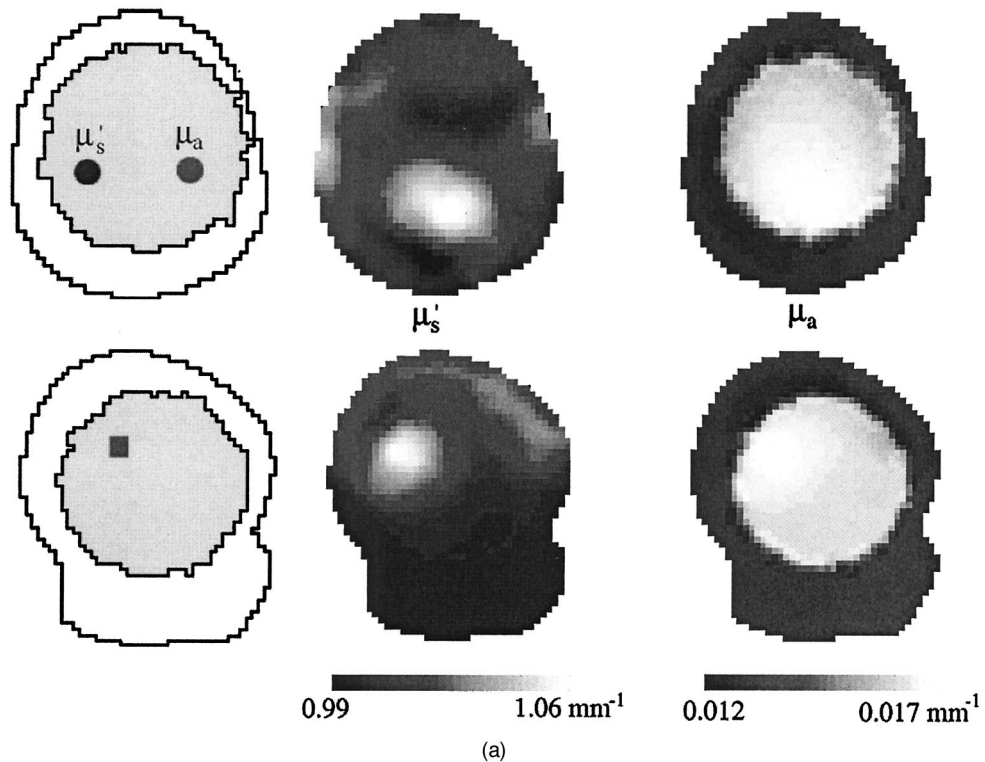


Fig. 5. (a) Reconstruction of the inhomogeneous phantom onto the head-shaped finite element mesh, starting from the calculated region properties. (b) Reconstruction of the inhomogeneous phantom onto the spherical finite-element mesh, starting from the calculated region properties.

ical mesh, particularly in the absolute region basis reconstruction, which is especially sensitive to modeling errors. More research on the incorporation of all aspects of *a priori* information into the reconstruction

algorithm, and more phantom studies, are required before the effect on the image of such *a priori* information can be fully understood.

The use of a hollow, fluid-filled phantom enables

different combinations of perturbations to be introduced easily and the regional properties to be varied, as was done here. Also, excellent reference data can be obtained from the same phantom, unlike the situation with solid phantoms when one phantom must be exchanged for another. However, this phantom is a simplification of a real neonatal head: There are no nonscattering regions to simulate the cerebrospinal fluid layer and ventricles, and the brain is modeled as a simple sphere. The effect of nonscattering regions on image quality is likely to be significant for absolute imaging,<sup>22</sup> although it may not be so important for difference imaging.<sup>23</sup> The irregular shape of the brain is likely to have little effect, apart from making the *a priori* information about the brain more difficult to obtain. New phantoms, with irregularly shaped nonscattering regions, are being built to examine these issues.

This research is an important step toward our goal of imaging the neonatal head. In particular, it suggests that it might be possible to obtain preliminary images with minimal *a priori* information about the internal structure of the head. Preliminary clinical trials of MONSTIR on babies in the neonatal unit at University College London Hospital are already underway using the techniques developed in this study.

We thank Liz Moore and Cathy Green at the National Hospital for Neurology and Neurosurgery, London, for performing the CT scan of the phantom. Funding was provided by the Wellcome Trust.

## References

1. B. Chance, E. Anday, S. Nioka, S. Zhou, L. Hong, K. Worden, C. Li, T. Murray, Y. Ovetsky, D. Pidikiti, and R. Thomas, "A novel method for fast imaging of brain function, non-invasively, with light," *Opt. Express* **2**, 411–423 (1998), <http://www.opticsexpress.org>.
2. D. A. Benaron, S. R. Hintz, A. Villringer, D. Boas, A. Kleinschmidt, J. Frahm, C. Hirth, H. Obrig, J. C. van Houten, E. L. Kermit, W.-F. Cheong, and D. K. Stevenson, "Noninvasive functional imaging of human brain using light," *J. Cereb. Blood Flow Metab.* **20**, 469–477 (2000).
3. S. R. Hintz, D. A. Benaron, A. M. Siegal, A. Zourabian, D. K. Stevenson, and D. A. Boas, "Bedside functional imaging of the premature infant brain during passive motor activation," *J. Perinat. Med.* **29**, 335–343 (2001).
4. D. A. Boas, T. Gaudette, G. Strangman, X. Cheng, J. J. A. Marota, and J. B. Mandeville, "The accuracy of near infrared spectroscopy and imaging during focal changes in cerebral hemodynamics," *Neuroimage* **13**, 76–90 (2001).
5. G. Taga, Y. Konishi, A. Maki, T. Tachibana, M. Fujiwara, and H. Koizumi, "Spontaneous oscillation of oxy- and deoxy-hemoglobin changes with a phase difference throughout the occipital cortex of newborn infants observed using non-invasive optical topography," *Neurosci. Lett.* **282**, 101–104 (2000).
6. A. Y. Bluestone, G. Abdoulaev, C. H. Schmitz, R. L. Barbour, and A. H. Hielscher, "Three-dimensional optical tomography of hemodynamics in the human head," *Opt. Express* **9**, 272–286 (2001), <http://www.opticsexpress.org>.
7. F. E. W. Schmidt, M. E. Fry, E. M. C. Hillman, J. C. Hebden, and D. T. Delpy, "A 32-channel time-resolved instrument for medical optical tomography," *Rev. Sci. Instrum.* **71**, 256–265 (2000).
8. S. R. Arridge, J. C. Hebden, M. Schweiger, F. E. W. Schmidt, M. E. Fry, E. M. C. Hillman, H. Dehghani, and D. T. Delpy, "A method for three-dimensional time-resolved optical tomography," *Int. J. Imaging Sys. Technol.* **11**, 2–11 (2000).
9. J. C. Hebden, E. M. C. Hillman, A. Gibson, N. Everdell, R. Yusof, D. T. Delpy, S. R. Arridge, T. Austin, and J. H. Meek, "Time resolved optical imaging of the newborn infant brain: initial clinical results," in *Biomedical Topical Meetings*, Vol. 71 of OSA Trends in Optics and Photonics Series (Optical Society of America, Washington, D.C., 2002), pp. 587–589.
10. H. Jiang, Y. Xu, and N. Iftimia, "Experimental three-dimensional optical image reconstruction of heterogeneous turbid media from continuous-wave data," *Opt. Express* **7**, 204–209 (2000), <http://www.opticsexpress.org>.
11. C. H. Schmitz, H. L. Graber, H. Luo, I. Arif, J. Hira, Y. Pei, A. Bluestone, S. Zhong, R. Andronica, I. Soller, N. Ramirez, S.-L. S. Barbour, and R. L. Barbour, "Instrumentation and calibration protocol for imaging dynamic features in dense-scattering media by optical tomography," *Appl. Opt.* **39**, 6466–6486 (2000).
12. F. E. W. Schmidt, J. C. Hebden, E. M. C. Hillman, M. E. Fry, M. Schweiger, H. Dehghani, H. D. T. Delpy, and S. R. Arridge, "Multiple-slice imaging of a tissue-equivalent phantom by use of time-resolved optical tomography," *Appl. Opt.* **39**, 3380–3387 (2000).
13. J. C. Hebden, H. Veestra, H. Dehghani, E. M. C. Hillman, M. Schweiger, S. R. Arridge, and D. T. Delpy, "Three-dimensional time-resolved optical tomography of a conical breast phantom," *Appl. Opt.* **40**, 3278–3287 (2001).
14. M. Firbank, M. Oda, and D. T. Delpy, "An improved design for a stable and reproducible phantom material for use in near-infrared spectroscopy and imaging," *Phys. Med. Biol.* **40**, 955–961 (1995).
15. P. van der Zee, M. Essenpreis, and D. T. Delpy, "Optical properties of brain tissue, in *Photon Migration and Imaging in Random Media and Tissues*, B. Chance and R. R. Alfano, eds., *Proc. SPIE* **1888**, 454–465 (1993).
16. C. R. Simpson, M. Kohl, M. Essenpreis, and M. Cope, "Near infrared optical properties of *ex-vivo* human skin and subcutaneous tissues measured using the Monte-Carlo inversion technique," *Phys. Med. Biol.* **43**, 2465–2478 (1998).
17. J. C. Hebden, F. M. Gonzalez, A. Gibson, E. M. C. Hillman, R. Md. Yusof, N. Everdell, D. T. Delpy, G. Zaccanti, and F. Martelli, "Assessment of an *in situ* temporal calibration method for time-resolved optical tomography," *J. Biomed. Opt.* **8**, 87–92 (2003).
18. J. Schöberl, "NETGEN—an advancing front 2D/3D mesh generator based on abstract rules," *Comput. Visual Sci.* **1**, 41–52 (1997).
19. M. Schweiger and S. R. Arridge, "Optical tomographic reconstruction in a complex head model using a priori region boundary information," *Phys. Med. Biol.* **44**, 2703–2721 (1999).
20. V. Ntziachristos, A. G. Yodh, M. D. Schnall, and B. Chance, "Optimization of diffuse optical spectroscopy of malignant and benign breast lesions," *Neoplasia* **4**, 347–354 (2002).
21. M. Schweiger, S. R. Arridge, M. Hiraoka, and D. T. Delpy, "The finite-element method for the propagation of light in scattering media: boundary and source conditions," *Med. Phys.* **22**, 1779–1792 (1995).
22. H. Dehghani, S. R. Arridge, M. Schweiger, and D. T. Delpy, "Optical tomography in the presence of void regions," *J. Opt. Soc. Am. A* **17**, 1659–1670 (2000).
23. H. Dehghani and D. T. Delpy, "Linear single-step image reconstruction in the presence of nonscattering regions," *J. Opt. Soc. Am. A* **19**, 1162–1171 (2002).